7-20-1987

Parallel Acoustic/Infrared Imaging of Single Crystal Surface and Subsurface Structure

F. Dacol
IBM T.J. Watson Research Center

S. Utterback
IBM T.J. Watson Research Center

Utah State University
MERRILL-CAZIER LIBRARY

PARALLEL ACOUSTIC/INFRARED IMAGING OF SINGLE CRYSTAL SURFACE AND SUBSURFACE STRUCTURE

F. Dacol and S. Utterback*

IBM T.J. Watson Research Center
P.O. Box 218
Yorktown Heights, NY 10598

Abstract

A modulated electron beam is used as a scanning thermal pump to examine the local surface and subsurface flaws of single crystal samples. The electron beam generated thermal waves are directly monitored by measuring the surface infrared emission while the longitudinal acoustic waves produced by thermal expansion are monitored simultaneously with a piezoelectric transducer. The results of point-by-point target scans are used to create images of the crystal surfaces. Contrasting images formed by the two techniques are compared as a function of electron beam modulation frequency. The infrared imaging technique is shown to evidence superior resolution.

*Address for correspondence:

S. Utterback
IBM T.J. Watson Research Center
P.O. Box 218
Yorktown Heights, NY 10598
Phone No. (914)945-1413

Introduction

The use of modulated electron beams to create detectable thermal waves as a means of probing materials' structure and properties has been studied for some time. The theories developed to explain the results of such experiments are, in general, well developed and well understood. Previous work has demonstrated the utility of infrared thermal imaging as a non-contact means of studying surface and near surface thermal properties.[4,6,8,13,16] Other related work has demonstrated the ability of thermally produced acoustic waves to likewise examine the surface and the internal structures of materials. [1,3,7,12] However, to the best of the authors' knowledge, there have not been any studies performed where both the surface thermal waves (as measured by infrared emission) and the thermally produced longitudinal acoustic waves (as measured with a piezoelectric transducer) were simultaneously but independently measured during a single experiment. This paper reports in part the results of a series of such experiments performed on single crystals of various chemical compositions.

The Experiments

The experiments were performed on single crystal samples of SiO_2, $BiVO_4$ and $SrTiO_3$, the pertinent physical parameter values of which are listed in Table 1. Single crystal samples were chosen to help eliminate the effects of deep internal structure on the acquired information. The crystals are first sliced into planar slabs using a diamond saw and then carefully cut into right circular cylinders using an ultrasonic impact grinder. The crystal fragments are then polished with submicrometer diamond compound and the resulting cylinders are approximately 2 millimeters in altitude and 3 millimeters in diameter. The PZT crystals used as piezoelectric transducers are prepared in the same fashion but with a smaller diameter to allow for an outer insulating sleeve.

In order to make the acoustic measurements at the same time as the infrared measurements, the specimen is mounted in an acoustic detector apparatus as described below.[2] The single crystal sample is cut into a cylinder (as described above) such that the cylinder wall is nearly flush with the inside wall of an open-ended copper cap in which it is placed (see Figure 1). Silver paint is used to assure good electrical contact between the cap and the sample. The bottom surface of the sample is

List of Symbols

A_i	atomic number of element i
A_r	time dependent radiating area
c	specific heat
C_i	weight fraction of element i
C_1	$3.743 \times 10^8 \ W \cdot \mu m^4 \cdot m^{-2}$
C_2	$1.439 \times 10^4 \ \mu m \cdot K$
d	Gruen range
D	thermal diffusivity
$E_{b\lambda}$	blackbody emissive power per λ per area
E_0	electron beam voltage
E_{el}	Elastic modulus
I_i	average ionization energy of element i
l	total electron path length
P_{e0}	absorbed electron beam power
$P_r(t)$	time dependent radiated power
P_{IR}	detected infrared power
PZT	lead zirconium titanate
r	magnitude of $\underset{\sim}{r}$
$\underset{\sim}{r}$	spherical coordinate radial vector
$\underset{\sim}{R}_G$	mean electron penetration depth or Gruen range
SEM	scanning electron microscope
S_T	thermal strain
S_M	mechanical strain
t	time
T	magnitude of $T(\underset{\sim}{r}, t)$
T_0	ambient temperature
$T(\underset{\sim}{r}, t)$	space and time dependent temperature
u(z,t)	z-component of local displacement
v	longitudinal velocity of sound
z	z-axis component of $\underset{\sim}{r}$
z_i	atomic number of element i
$\hat{z}$	beam axis unit vector
α	thermal expansion coefficient
β	$(1 - 1/\nu^2)^{1/2}$
γ	complex propagation constant
ε	emissivity
ζ	infrared collection/detection efficiency
η	thermal energy source density function
ν	$E_0/511 + 1$
Θ	magnitude of $\Theta(\underset{\sim}{r}, t)$
$\Theta(\underset{\sim}{r})$	spatial part of $\Theta(\underset{\sim}{r}, t)$
$\Theta(\underset{\sim}{r}, t)$	space and time dependent temperature
κ	thermal conductivity
λ	wavelength
ρ	density
σ	Stefan-Boltzman constant
σ_M	mechanical stress
σ_T	thermal stress
μ_λ	infrared energy density per λ per volume
ω_0	modulation frequency

contacted to the top surface of a silver coated PZT (lead zirconium titanate) crystal, the piezoelectric transducer, mounted in an insulating sleeve (to electrically isolate it from ground) which is flush with the inside wall of the cap. The cap is threaded and screws onto a copper base which serves as the specimen stub. Inside the base is an insulated electric lead which, through a drop of silver paint, contacts the bottom surface of the PZT crystal. The lead serves as a spring such that when the cap is tightened the sample and the PZT crystal are pressure fit together. The entire holder is mounted in the SEM
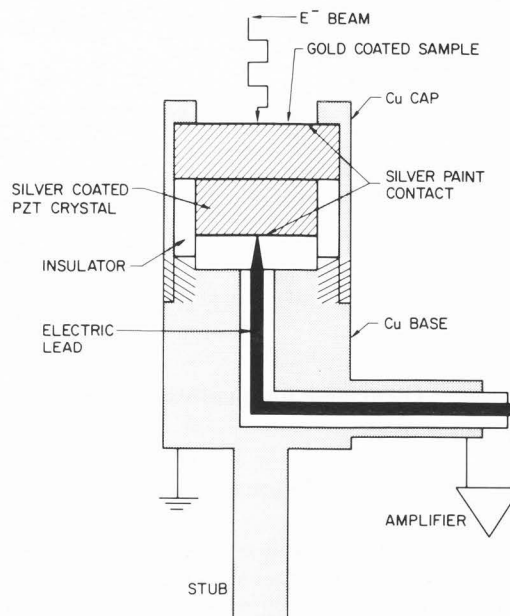

Fig. 1: The sample holder/acoustic detector apparatus.

Table 1: Values of pertinent physical parameters.

MATERIAL	$\kappa \ (\frac{W}{cm \cdot K})$	$\rho \ (\frac{g}{cm^3})$	$C \ (\frac{cal}{g \cdot K})$	$D \ (\frac{cm^2}{s})$
$SrTiO_3$	0.08	5	0.13	0.03
$BiVO_4$	0.03	6.5	0.07	0.015
SiO_2	0.015	2.6	0.17	0.008

and an electrical connection to the outside of the microscope made through a hermetically sealed bulkhead feedthru. The above described device allows us to detect the thermally produced longitudinal acoustic waves which are transmitted through the sample and reach the PZT crystal by measuring the electrical signal resulting from the crystal's piezoelectric response.

The thermal pump in our experiments is the electron beam from a scanning electron microscope. The experimental setup used to measure infrared emissions produced by surface thermal waves has been previously described[6,8,17]. For convenience, a diagram of the apparatus taken from reference 17 has been reproduced in Figure 2. A schematic of the infrared detector/collector apparatus is shown in Figure 3. Note that in the present detector/collector configuration the collecting ellipsoidal mirror has been tilted in order to bring the detector itself above the target focal plane. This modified construction allows for the unrestricted inspection of large samples.

The experiments are carried out in the following fashion. The acoustic detector device is positioned such that the sample is roughly at the infrared collection optics focal point while viewing the sample using the SEM in conventional fashion. The
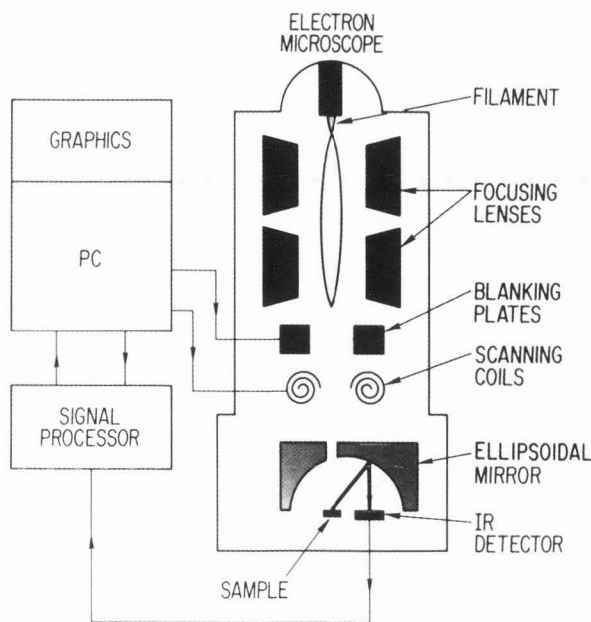
Fig. 2: The scanning electron microscope apparatus.
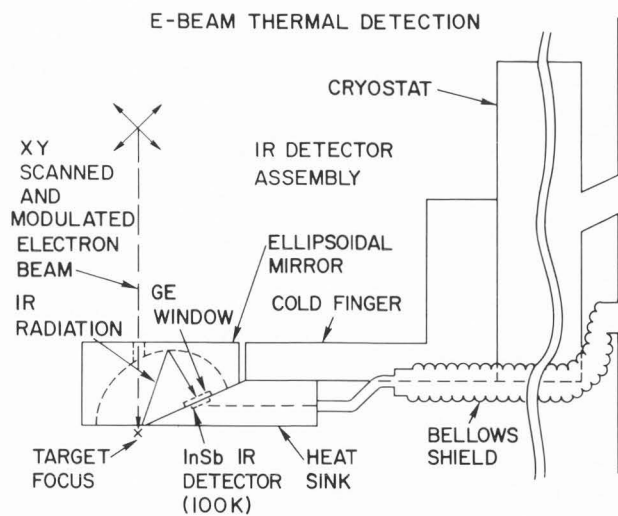
E-BEAM THERMAL DETECTION

Fig. 3: The infrared collector/detector apparatus.

fine focus adjustment is then made by maximizing the infrared signal using the vertical specimen position adjustment control. Typically a beam voltage of 10 to 20 keV and a beam current of up to several hundred nanoamps are employed. This produces a maximum temperature rise in the beam absorbing volume which is on the order of 100K (see Equation 8).

The entire experiment is run using an **IBM PC** through a Tecmar Labmaster and two lock-in amplifiers, one of which is used to process the signal from the infrared detector and the other the signal from the acoustic detector. The computer controls the position of the beam, collects data at each position, and stores them. It also controls the settings of the lock-in amplifiers including the frequency of the lock-ins' internal oscillators, the time constants, Q-factors, and filter frequencies. The internal oscillator of one lock-in is used to reference the internal oscillator of the second lock-in and serves as well to control a square-wave electron beam modulator driver. During the image acquisition the dwell time per pixel is set to be longer than the Q-factor/modulation frequency ratio and lock-in time constants.

The in-phase and out-of-phase data collected and stored by the PC may be processed to calculate the phase and the amplitude of the thermal and acoustic signals measured at each pixel of the electron beam sweep. The phase information is carefully corrected for frequency-dependent phase shifts introduced by the apparatus. The resulting information may be displayed in the form of a two dimensional image using a graphics monitor as in the experiments described here, or individual line scans may be reconstructed and displayed.

Theory

Thermal wave imaging involves applying heat pulses to a sample while monitoring its thermal response. In the present case the specimen surface is heated with a focused electron beam which is modulated on and off to produce the thermal waves. One thermal wave detection approach we employ is to collect and detect the time dependent integrated surface infrared emission. This provides a direct means of monitoring the surface temperature in the region affected by the thermal waves. The second approach to thermal wave detection we use is to measure the acoustic wave that results from the thermal expansion of the locally heated region. This provides an indirect means of monitoring the temperature of the heated region below the sample surface.

Since the thermal wave produced in the target sample is exponentially damped as a function of distance (measured in thermal wavelengths) from the initially heated source, the surface infrared emission and the thermally generated acoustic signal both contain information about the thermal properties of the material within about one thermal wavelength of where the electron beam penetrates (however, as will be demonstrated the infrared approach is actually sensitive to a smaller region than the acoustic approach). Therefore, by varying the period of the electron beam modulation it is possible to obtain information from varying depths below the surface. In principle, thermal wave mapping of the same area using different modulation frequencies can provide sufficient information to reconstruct a three dimensional image of the thermal properties of the target; however, in the present case the information obtained is restricted to the region within about 100 micrometers of the surface where there are thermally detectable flaws.

The principal intent of this paper is to experimentally demonstrate the differences in the resolution of surface detail attainable with the two standard detection approaches described above. There is a great deal of controversy concerning the theory behind the physics involved, particularly in the case of acoustic wave generation. We do not choose to take sides in this controversy at this time. However, a simple theory describing the underlying physics of thermal expansion acoustic wave generation and thermal infrared radiation generation are

presented below. The assumptions made concerning the experimental conditions are as follows;[6,12]

1. Homogeneous, isotropic medium with a planar surface.

2. Semiinfinite solid (in the positive Z-direction).

3. Homogeneous beam energy profile.

4. Uniform energy dissipation at the surface.

In the case of an isotropic homogeneous target, heat diffusion can be described by [5]

$$\nabla^2 T(\underset{\sim}{r}, t) = \frac{1}{D} \frac{\delta}{\delta t} T(\underset{\sim}{r}, t) - \frac{1}{\kappa} \eta(\underset{\sim}{r}, t) \tag{1}$$

where $T(\underset{\sim}{r}, t)$ is the space and time dependent temperature at position $\underset{\sim}{r}$ and $\eta(\underset{\sim}{r}, t)$ is a source density function. The thermal diffusivity

$$D = \frac{\kappa}{\rho c} \tag{2}$$

depends on the thermal conductivity, κ, the density, ρ, and the specific heat, c, of the system. $T(\underset{\sim}{r}, t)$ can be divided into a space and time invariant term T_0 (which may be considered to represent the ambient temperature) and a time and space dependent term $\Theta(\underset{\sim}{r}, t)$ such that

$$T(\underset{\sim}{r}, t) = T_0 + \Theta(\underset{\sim}{r}, t) \tag{3}$$

In the remaining calculations it is assumed that the magnitude of $\Theta(\underset{\sim}{r}, t)$ is small compared to T_0, and that

$$\eta(\underset{\sim}{r}, t) = \eta(\underset{\sim}{r}) e^{j\omega_0 t} \tag{4}$$

and

$$\Theta(\underset{\sim}{r}, t) = \Theta(\underset{\sim}{r}) e^{j\omega_0 t}. \tag{5}$$

where ω_0 is the fundamental component of the modulation frequency. Equations 4 and 5 are equivalent to restricting our analysis to the fundamental Fourier component of both the modulated thermal pump and the time dependent temperature distribution. These terms can be shown to dominate the system response.[6,8,17]

Assuming the surface thermal wave propagates with circular symmetry away from $\hat{z}$, the beam axis, and employing the assumptions described in the preceding paragraph, the actual temperature rise of the substrate surface in the vicinity of the thermal pump is given by:

$$\Theta(\underset{\sim}{r}, t) = \frac{P_{e0}}{4\pi\kappa} \cdot \frac{e^{-\gamma r}}{r} \cdot e^{j\omega_0 t} \tag{6}$$

at distances r (the magnitude of $\underset{\sim}{r}$) which are large compared to R_G, the beam absorption length. Here P_{e0} is the absorbed power and γ is the complex propagation constant given by

$$\gamma = (1 + j) \cdot \sqrt{\frac{\omega_0}{2D}}. \tag{7}$$

Assuming an approximately Gaussian beam absorption profile about the mean electron penetration point the temperature change within the electron beam absorbing volume can be approximated by

$$\Theta(r = 0, t) \cong \frac{P_{e0}}{2\sqrt{2} \kappa \cdot R_G} e^{j\omega_0 t} \tag{8}$$

where R_G is the average electron penetration depth. Here it is assumed that the heated volume is at least several times larger than the beam absorbing volume. The average electron penetration depth, or Gruen range, can be calculated from Equation (9) [9]

$$R_G(\mu m) = 0.04 \frac{E_0^{1.75}}{\rho} \tag{9}$$

where E_0 is the electron beam energy (in kilovolts). Monte Carlo calculations show that at $E_0 = 20$ keV, roughly 80% of the incident beam energy is deposited in a small (several cubic micrometers) volume of the sample and is rapidly (< 1 nsec) thermalized. [15]

Infrared thermal wave imaging involves collecting and detecting the infrared emission from the surface of the sample. Since most of the materials we have examined are opaque in the infrared, the infrared emission is necessarily restricted to a region within roughly 10 micrometers of the surface (SiO_2 is an exception). Our apparatus allows us to collect the total time dependent surface emission and focus it onto an infrared detector with a limited wavelength response. The infrared power $P_r(t)$ radiated from the sample surface and collected by our apparatus can be calculated from the Stefan-Boltzman law[6]

$$P_r(t) = \iint_{A_r} \varepsilon \cdot \sigma \cdot T^4(\underset{\sim}{r}, t) dA_r \tag{10}$$

where ε is the emissivity, σ the Stefan-Boltzman constant, and A_r the time dependent radiating area. Imposing the conditions described above (i.e., small Θ, axial symmetry, and fundamental Fourier components), the power radiated from the surface in the vicinity of the thermal source can be described by:

$$P_r(t) \cong 8\pi \cdot \varepsilon \cdot \sigma \cdot T_0^3 \int_{r=0}^{\infty} \Theta(r, z = 0) e^{j\omega_0 t} \cdot r dr. \tag{11}$$

Substituting in Equation (6) from above and integrating, the solution for $P_r(t)$ in homogeneous, isotropic materials becomes

$$P_r(t) = \frac{8 \cdot \varepsilon \cdot \sigma T_0^3}{\kappa} \cdot \frac{P_{e0} \text{top}}{\pi} \cdot \frac{1}{\gamma + R_G} \cdot \frac{1}{\gamma} \cdot e^{j\omega_0 t}. \tag{12}$$

Finally, in the limit that the absorption volume << heated volume (or $R_G \rightarrow 0$), Equation (12) becomes

$$P_r(t) = \frac{8 \cdot \varepsilon \cdot \sigma T_0^3}{\kappa} \cdot \frac{P_{e0}}{\pi} \cdot \frac{1}{\gamma} \cdot e^{j\omega_0 t}. \tag{13}$$

These equations (10 - 13) contain both the spatial and the time dependence of the measured infrared signal.

Assuming an emissivity of unity, the radiated power can be redefined in terms of temperature and the spectral wavelength, the energy density per unit wavelength per unit volume is given by [10,11]

$$\mu_\lambda = \frac{8\pi h c \lambda^{-5}}{\left(e^{hc/k\lambda T(\underset{\sim}{r}, t)} - 1\right)}. \tag{14}$$

$E_{b\lambda}$, the blackbody emissive power per λ per unit area, will be given by:

$$E_{b\lambda} = \mu_\lambda c/4$$
$$= C_1\lambda^{-5}\left(e^{C_2/\lambda T(\underline{r}, t)} - 1\right)^{-1} \qquad (15)$$

where $C_1 = 3.743 \times 10^8 \ \text{W} \cdot \mu m^4 \cdot m^{-2}$, $C_2 = 1.439 \times 10^4 \ \mu m \cdot K$, T is in units K and λ in units μm. We have ascertained that for temperatures between 350K and 450K, the most sensitive conventional infrared detectors are the photovoltaic InSb detectors. These detectors ordinarily operate in the wavelength range from about 1.5 to 5.5 μm. Using Eq. (16) it is possible to calculate P_{IR}, the infrared power in the wavelength range the InSb detector 'sees',

$$P_{IR} = \int_{A_r} \int \int_{\lambda=5.5\mu m}^{\lambda=1.5\mu m} \frac{\zeta C_1\lambda^{-5}}{\left(e^{C_2/\lambda T(\underline{r}, t)-1}\right)} \, dA_r d\lambda \qquad (16)$$

where ζ is the detection efficiency of the infrared detection system. The detection efficiency will depend on, among other things, the collection efficiency and reflection and absorption losses. We estimate that roughly 50 % of the emitted radiation reaches the detector.

The actual signal response of the detector can be calculated from an integrated convolution of Equation 16 with the spectral responsivity of the specific detector used. Since it is not ordinarily possible to define an explicit function describing the detector responsivity, this generally involves a point-by-point numerical integration using experimentally determined values. The fact that the wavelength response of the detector is limited to short wavelengths makes the detector response to surface temperature non-linear, that is it is much more sensitive to the hottest area of the heated region. We argue that this is largely responsible for the superior resolution we can achieve with the infrared detection approach.

The analysis provided above describes the system response in the case of an isotropic, homogeneous medium with a planar surface. The result of Equation (13) is that both the in-phase and quadrature components of the detected infrared signal should always remain equal , independent of ω_0 (as long as $\gamma^{-1} << R_G$), giving a phase shift of $\frac{\pi}{4}$. The amplitude of the signal should scale as $\sqrt{\omega_0^{-1}}$. However, the presence of flaws at the surface of the sample presents a deviation from ideality which results in a differential signal that provides a means of defect detection.

In electron beam thermally induced acoustics measurements the pressure wave created by the local thermal expansion is measured in some fashion. In the present case we are detecting the longitudinal acoustic modes created at the surface which propagate through the sample and produce an electrical response in the PZT crystal. Due to the relative complexity of the geometrical arrangement used in our acoustic detection apparatus the only assumption we can make regarding the detector response is that it is monotonic with respect to the amplitude of the impinging acoustic waves. Testing of the acoustic detector has demonstrated that the detector itself responds to thermal pumping by the electron beam in the predicted manner,

i.e., the greater the input power the greater the signal. A review of a simple theory describing thermally produced acoustic waves is detailed below. Here we have made the same assumptions as above in reviewing infrared thermal wave detection.

The strain induced by the local electron beam heating is given by:[12]

$$S_T = \left[\frac{\delta u(z,t)}{\delta z} \right] = \alpha\Theta(z,t) \qquad (17)$$

where $u(z,t)$ is the z-component of the local displacement and α is the linear thermal expansion coefficient. The thermal expansion strain results in a thermal stress given by:

$$\sigma_T = -E_{el} \cdot \alpha\Theta(z,t) \qquad (18)$$

where E_{el} is the elastic modulus For completeness sake we also include the mechanical stress σ_M given by

$$\sigma_M = \rho \cdot v^2 \cdot s_M \qquad (19)$$

where v is the longitudinal velocity of sound and s_M equals the mechanical strain. From the equations of stress above can be derived the local equation of motion given by:

$$\frac{\delta^2 u}{\delta t^2} = v^2 \frac{\delta^2 u}{\delta z^2} - \frac{\alpha E_{el}}{\rho} \cdot \frac{\delta\Theta(z,t)}{\delta z}. \qquad (20)$$

This approximation breaks down in the long wavelength limit. Here we have not included the possible role of the acoustic detector/sample geometry in influencing the detected signal amplitude, however, these considerations are not anticipated to affect the resolution of the acquired images.

A straightforward analysis (based on the assumptions previously described) of the infrared emission and the acoustic transmission resulting from local heating of a sample predicts that both the infrared and the acoustic signals should increase or decrease together as a function of the properties of the sample. Interestingly, as shown below this is not always the case.

Results

The calculated values of the thermal wavelengths d(l) (as given by the e^{-1} values for Θ as a function of t and ω_0 using Equation 6) for the materials examined are presented in Table 2. The corresponding values for the acoustic wavelengths are several orders of magnitude larger but are not directly considered since the resolution in the acoustic images is determined primarily by the thermal source size, i.e., the volume contained within approximately one thermal wavelength. It will be seen that the effective thermo-acoustic source size may be substantially different from the thermal infrared source size. In most experiments the acoustic signal-to-noise ratio was at least an order of magnitude better than the infrared signal-to-noise, although at very low modulation frequencies the two were roughly equivalent. The change in acoustic signal-to-noise is due in part to the frequency dependence of the boundary conditions.

The values for the electron penetration depth d and the total electron path length l are presented in Table 3 where d = R_G and l is given by Equation 21[14]

Table 2: Thermal wavelength (μm) vs. modulation frequency.

MATERIAL	100 Hz	1 kHz	10 kHz	100 kHz
SrTiO$_3$	98	31	9.8	3.1
BiV O$_4$	69	22	6.9	2.2
SiO$_2$	51	16	5.0	1.6

Table 3: Electron penetration (μm) vs. beam energy.

MATERIAL	l (μm) 9.7 KeV	l (μm) 19 KeV	d (μm) 9.7 KeV	d (μm) 19 KeV
SrTiO$_3$	0.69	3.2	0.43	1.4
BiV O$_4$	0.49	2.2	0.33	1.1
SiO$_2$	1.5	7.3	0.80	2.6

$$1(\mu) = \int_0^{E_o} \left[0.3076 \frac{\rho}{\beta^2} \sum_i C_i \frac{Z_i}{A_i} \left\{ \ln\left(\frac{E_0}{I_i} \sqrt{\nu + 1} \right) + \right. \right.$$
$$\left. \left. 0.153 - \frac{1}{2}\beta^2 + \frac{1}{16}\left(\frac{\nu - 1}{\nu} \right)^2 - 0.693 \frac{2\nu - 1}{2\nu^2} \right\} \right]^{-1} dE_0 \quad (21)$$

For convenience sake we will refer primarily to the results of the experiments performed on SrTiO$_3$, the results of experiments on SiO$_2$ and BiVO$_4$ are qualitatively similar. The images presented in Figures 4 - 7 were obtained using an accelerating voltage of 19 keV and a beam current of about 200 nanoamps. In all figures the magnitude of the detected signal is displayed, i.e., the square root of the sum of the squares of the in-phase and quadrature components measured by the lock-in amplifier.

Figures 4(a) and 4(b) show images generated from infrared and acoustic signal measurements, respectively, generated using a modulation frequency of 100 kHz. In both images striations on the surface due to fracture lines along cleavage planes are clearly visible. Note the somewhat clearer definition in the infrared signal as well as the reversed striation contrast in the acoustic image. As previously noted, the signal-to-noise ratio is substantially better for the acoustic measurements.

Figures 5(a) and 5(b) show the corresponding images recorded using a modulation frequency of 10 kHz. Here the thermal wavelength is of the same order as the cross section of structures being measured, about 10 micrometers. The resolution of the acoustic image is already beginning to degrade significantly whereas the detail in the infrared image is rela-

Fig. 4(a): The thermal infrared image of SrTiO$_3$ surface structure. Modulation frequency equals 100 kHz. Unit spacing equals 100 micrometers.

Fig. 4(b): The thermal acoustic image of SrTiO$_3$ surface structure. Modulation frequency equals 100 kHz. Unit spacing equals 100 micrometers.

Fig. 5(a): The thermal infrared image of SrTiO$_3$ surface structure. Modulation frequency equals 10 kHz. Unit spacing equals 100 micrometers.

Fig. 5(b): The thermal acoustic image of SrTiO$_3$ surface structure. Modulation frequency equals 10 kHz. Unit spacing equals 100 micrometers.

Fig. 6(a): The thermal infrared image of SrTiO$_3$ surface structure. Modulation frequency equals 1 kHz. Unit spacing equals 100 micrometers.

Fig. 6(b): The thermal acoustic image of SrTiO$_3$ surface structure. Modulation frequency equals 1 kHz. Unit spacing equals 100 micrometers.

tively unchanged. Notice the appearance of a subsurface void in the middle of the imaged area. This is a structure which is not visible in an ordinary SEM view.
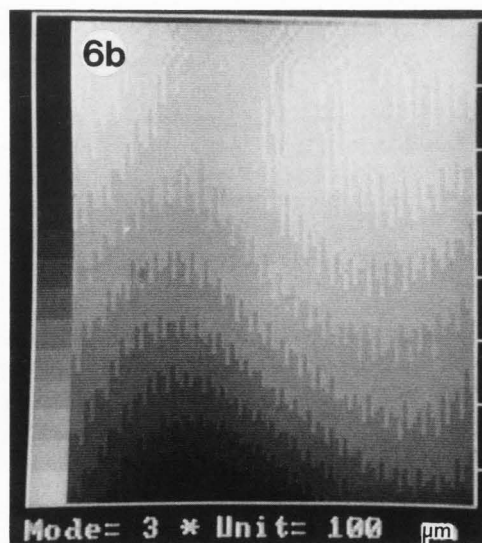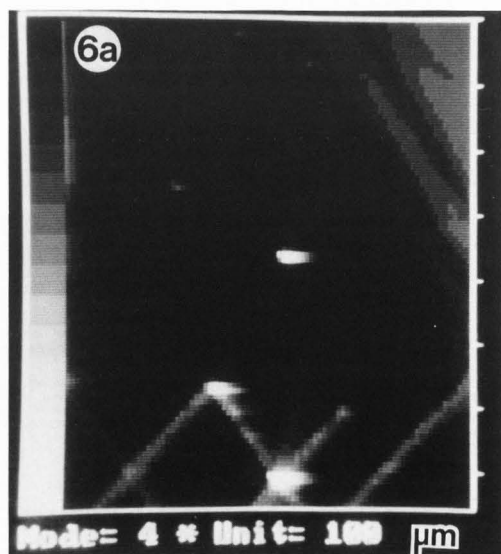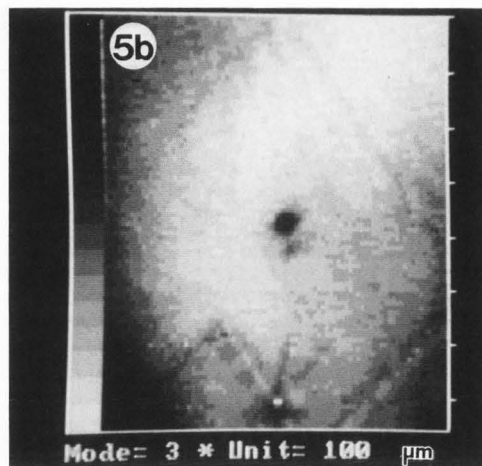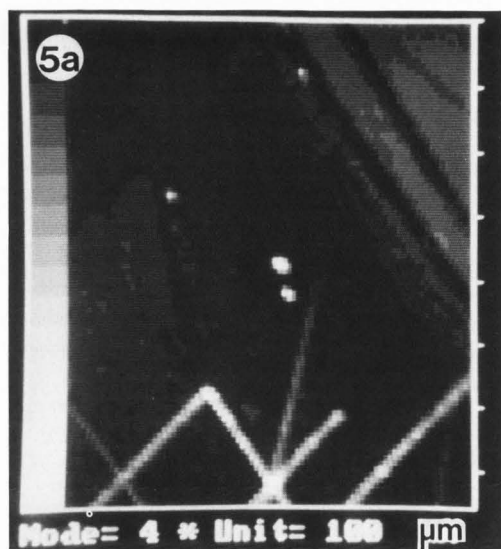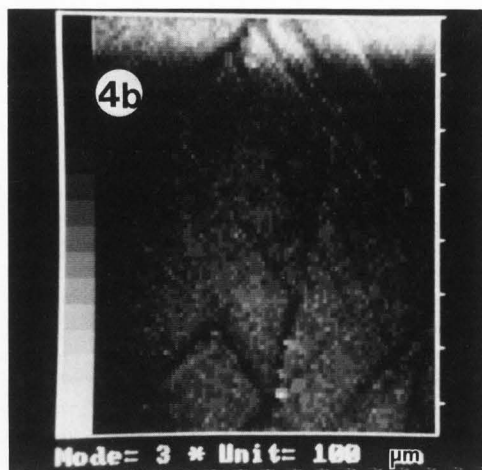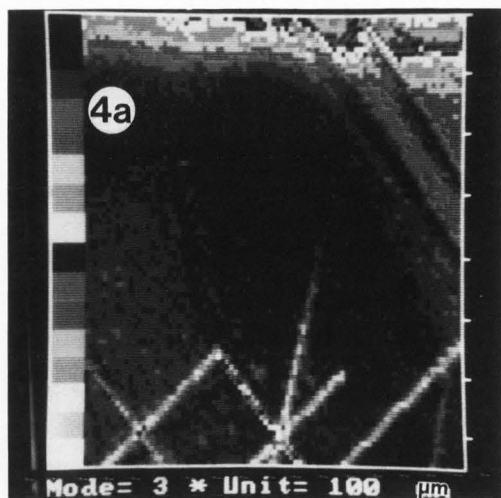
In Figures 6(a) and 6(b) the corresponding images acquired using a modulation frequency of 1 kHz are displayed. At this frequency there is almost no hint of the structures seen at higher modulation frequencies in the acoustic image. The infrared image still shows most of the previous detail, although a degradation in resolution is starting to become evident.

Finally, in Figures 7(a) and 7(b) the corresponding images acquired using a modulation frequency of 0.1 kHz show the structural detail is completely absent in the acoustic image and is significantly degraded in the infrared image.

Discussion

The images obtained from the thermal infrared technique generally show greater resolution of surface structure than the thermal acoustic technique. This is particularly apparent at low modulation frequencies where the thermal wavelength is much larger than the electron penetration depth. (See Tables 2 and 3). Since the loss of resolution in the acoustic images is not attributable to significant degradation of the signal-to-noise ratio we measure, it may be due in part to information simply being washed out by the bulk sample which the acoustic wave must propagate through.

A more significant consideration is as follows. The acoustic signal generation is linearly dependent on the local temperature rise, so that the volume region producing the acoustic signal may be significantly larger than the volume contained within a thermal wavelength (See Discussion with Reviewers, Reference 12). In contrast, the infrared emission intensity goes as the fourth power of the local temperature times the locally affected surface area. In the simple theoretical analysis provided above it was assumed that the time dependent temperature fluctuation is sufficiently small that only the first order AC term need be considered. However, under the operating conditions actually employed the magnitude of the time

Mode= 3 * Unit= 100 μm

Mode= 3 * Unit= 100 μm

Mode= 4 * Unit= 100 μm

Mode= 3 * Unit= 100 μm

Mode= 4 * Unit= 100 μm

Mode= 3 * Unit= 100 μm

dependent temperature fluctuation is a significant fraction of the ambient temperature (about 1/3 within the beam absorbing region) and the higher order terms which have not been directly considered begin to have a significant effect. Meanwhile, the actual measured infrared signal intensity will display an even higher order temperature dependence than the total integrated infrared intensity due to the limited wavelength sensitivity of the InSb detector. A temperature rise of 100K at an ambient temperature of 300K will produce a factor of ten increase in emission intensity per unit area at $\lambda = 5\mu m$ (the upper wavelength detection limit of an InSb detector) while the emission intensity per unit area one thermal wavelength away from the source has only increased by a factor of two. The difference increases rapidly (as $\exp\frac{C_2\Theta}{\lambda k T_0 T}$ where Θ is the magnitude of the local temperature rise) as the monitored wavelength decreases. Therefore, the region producing an infrared signal to which the detector is sensitive is actually significantly smaller than that encompassed by a thermal wavelength. This provides the infrared technique a substantial resolution advantage in imaging surface and near surface structure in spite of inferior signal-to-noise. Infrared imaging of course has a further advantage in that it is a non-contact method and no special sample preparation is required as the technique is employed in our current system, although conductive coatings are generally used. This is in contrast to the extensive sample preparation required for thermal acoustic measurements.

The physical mechanism responsible for the inverted signal intensity change noted in the acoustic surface structure images is not completely understood. It is clear from the infrared images that the surface flaws we measure are trapping thermal energy and producing local hot-spots. The simple acoustic generation theory reviewed above would predict an increase in the acoustic signal in these areas, the reverse of what is actually seen. It is the authors' opinion the most likely explanation of the contrast reversal is that there exist in these regions geometrical degrees of freedom that allow the heated volume to freely expand without producing the stress fields that result in the propagation of an acoustic signal. Whereas this explanation may at first appear somewhat tenuous, it is reasonable to suppose that at the surface the thermally expanding region can relieve stress through surface deformation. When surface flaws cause the surface profile to deviate from planarity it provides more possibilities for deformation to relieve stress. This may explain why the detected surface flaws get hotter but produce a smaller acoustic signal. Further testing is needed in order to clarify the underlying causes of this observation.

Conclusion/Summary

We have demonstrated the ability to simultaneously acquire both thermal infrared and thermal acoustic information from a sample using the electron beam of a modified scanning electron microscope as a thermal pump. The noncontact infrared measurements were made using an ellipsoidal mirror and a shielded InSb infrared detector while the acoustic measurements were made through the use of a piezoelectric transducer contacted to the bottom surface of the specimen. The results demonstrated the superior resolution which can be achieved using the infrared approach due to the non-linear sample temperature dependence of the infrared detector response. This study also suggests the need for further work to clarify the underlying mechanisms responsible for the contrast differences noted in the images obtained using the two techniques.
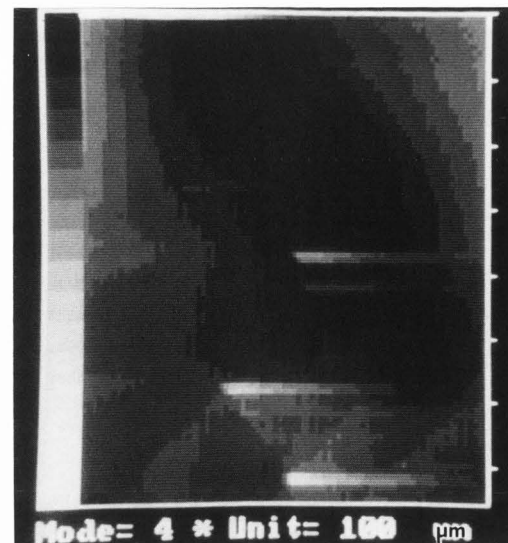

Fig. 7(a): The thermal infrared image of SrTiO3 surface structure. Modulation frequency equals 0.1 kHz. Unit spacing equals 100 micrometers.
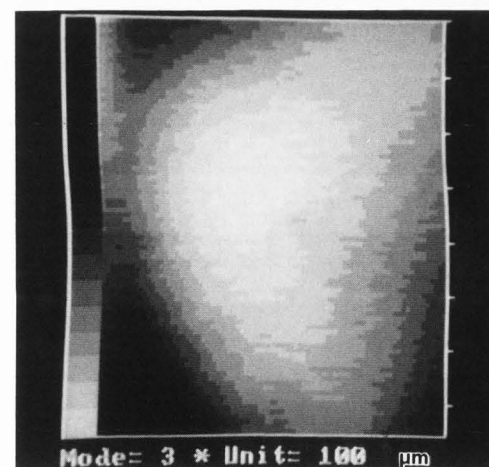

Fig. 7(b): The thermal acoustic image of SrTiO3 surface structure. Modulation frequency equals 0.1 kHz. Unit spacing equals 100 micrometers.

Acknowledgements

References

1. Balk LJ, Kultscher N. (1983). Scanning electron acoustic microscopy. BEDO **16**, 107-120.

2. Baumann T, Dacol FH, Melcher, RL. (1983). Transmission thermal-wave microscopy with pyroelectric detection. Appl. Phys. Lett. **43**, 71-73.

3. Brandis E, Rosencwaig A. (1980). Thermal wave microscopy with electron beams. Appl. Phys. Lett. **37**, 98-100.

4. Busse G. (1980). Photothermal transmission probing of a metal. Infrared Phys. **20**, 419-422.

5. Carslaw HS, Jaeger JC. (1973). *Conduction of Heat in Solids*, Oxford University Press, Clarendon, 10-49.

6. Dacol FH, Ermert H, Melcher RL. (1985). Non-contact thermal-wave imaging with infrared detection. Scanning Electron Microsc. 1985; II: 627-630.

7. Davies DG. (1983). Scanning acoustic electron microscopy. Scanning Electron Microsc. 1983; III: 1163-1176.

8. Ermert H, Dacol FH, Melcher RL, Baumann T. (1984). Advances in non-contact thermal-wave imaging with infrared detection. Appl. Phys. Lett. **44**, 1136-1138.

9. Everhart TE, Hoff PH. (1971). Determination of kilovolt electron energy dissipation vs penetration distance in solid materials. J. Appl. Phys. **42**, 5837.

10. Holman JP. (1981). *Heat Transfer*. McGraw-Hill, New York, 305-316.

11. Kalenshar BE. (1984). Blackbody radiation from spheres and cubes with application to the rapid solidification of microspheres. J. Appl. Phys. **56**, 1347-1354.

12. Kultscher N, Balk LJ. (1987). Signal generation and contrast mechanisms in scanning acoustic microscopy. Scanning Microsc. **1**(1) 33-43.

13. Nordal PE, Kanstead SO. (1979). Photothermal radiometry. Phys. Scr. **20**, 659-662.

14. Robinson JW. (1978). *Handbook of Spectroscopy*, I. The Chemical Rubber Co., Boca Raton, FL. 249.

15. Rosenfield MG. (1984). *Analysis of Backscattered Electrons for X-Ray Mask Inspection*, Ph.D. Thesis Monte Carlo Program. University of California, Berkeley.

16. Tam A, Sullivan SA. (1983). Remote Sensing Applications of Photothermal Radiometry. Appl. Phys. Lett. **43**, 333-335.

17. Utterback SG, Dacol FH, Ermert H, Melcher RL. (1985). Thermal Coupling of Particulates to Substrates. Appl. Phys. Lett. **46**, 1054-1056.

Discussion with Reviewers

<u>D.G. Davies:</u> I accept your discussion, but I'm afraid I don't find the images to be a convincing experimental demonstration. Could you give some numerical estimates of the experimental resolutions which you are observing, and the measurement criteria you use for the estimates? Incidentally, I feel that the images demonstrate primarily a relative decrease (with frequency) in sensitivity of the acoustic technique, rather than in resolution. This is to be expected, since the significantly-heated radius varies as $\omega^{-0.5}$, so that the acoustic-signal producing volume should go up as $\omega^{-1.5}$ (as the frequency goes down). Thus for features smaller than the heated volume (i.e., below, say 10kHz) the small contrast (differential) signal will become overwhelmed by the signal from the homogeneous bulk of the heated volume. The contrast

signal/noise may fall by as much as a factor of $(100)^{1.5} = 1000$ in going from 100 kHz to 1kHz even though the total S/N remains constant, which probably accounts for the disappearance of the acoustic image contrast. This makes the infrared images all the more remarkable and useful since as you note, they select the signal from just a plane (rather than a volume) which is (probably in this case) close to the contrast-producing features. Thus, under conditions such as those you observed, the infrared images probably show a significant advantage in sensitivity (despite straightforward S/N considerations) as well as in resolution.

<u>Authors:</u> We agree that it is unfortunate we are not in a position to share some more convincing images illustrating our points. The apparent resolution of the acoustic images are on the order of micrometers at 100 kHz. The apparent resolution of the infrared images at the same frequency are on the order of a tenth of a micrometer as evidenced by the contrast observed in point-by-point line scans taken with pixel resolution on that scale.[17] The beam spot size under the conditions ordinarily employed is about 0.2 micrometers. However, both the region heated by the electron beam and the linear dimensions of the spatial region required for emission of infrared photons of the wavelength we measure are of the order of a micrometer or greater.

The mechanistic details of the acoustic signal generation are the subject of wide debate and it is not the intent of this paper to directly address this issue. However, we feel we have convincingly demonstrated that the resolution achievable using our standard radiometric thermal wave detection technique is superior to the resolution which can be achieved using the conventional acoustic detection method described under the conditions reported in the paper. The authors agree with your discussion concerning the causes of the acoustic signal resolution degradation, although we would like to point out that the measured S/N was never better using the infrared detection approach under any of the conditions which we employed.

<u>D.G. Davies:</u> Certain effects in figs. 6a and 7a look like image streaking due to the scan being too fast. Did your computer control lock-in time constants as well as the image scan rate, and can you give us some idea of these parameters at the different frequencies?

<u>Authors:</u> The Q-factor and the time constant of the lock-in amplifier were set to give an effective time constant of 10 milliseconds at all modulation frequencies. The image acquisition time was then set to at least 10 milliseconds per pixel. However, as you have noted when the lock-in is overloaded it can take susbstantially longer than this to relax. Running the amplifier at a lower gain causes much of the contrast in the rest of the image to be lost.

<u>N. Kultscher:</u> You contact the bottom surface of the PZT crystal with a drop of silver-paint to the electrical lead. Why don't you use a metallic block? It should supply a good electrical contact and help to avoid sound reflections back into the transducer.

<u>Authors:</u> The silver paint when dried effectively acts as a silver block. We have in the past experimented with various arrangements and found this to be satisfactory.

<u>N. Kultscher:</u> Is it possible to separate various sound generation mechanisms (for example the thermal - and the piezoelectric coupling) with the simultaneous measurements of

infrared and acoustic images?

Authors: The samples were chosen to provide a fairly unambiguous situation for studying the differences in resolution of surface detail using the thermo-acoustic and the thermal infrared detection approaches. With the exception of SiO_2, we believe the materials studied not to be piezoelectric since they are centrosymmetric at room temperature. We have been unable so far to find these materials described in the literature as piezoelectric, but would be interested in any studies with which you are aware that suggest otherwise. It would certainly be of great interest to extend this work to help advance the undersanding of acoustic signal generation as per your suggestion.

N. Kultscher: The explanation of the contrast reversal postulates degrees of freedom in solids without coupling to the rest of the crystal. Can you explain the appearance of this non coupling behaviour of the degrees of freedom?

Authors: It has been noticed in this and other work that when a heated region is allowed to expand freely (i.e. is unrestrained) the acoustic signal intensity is attenuated. The coupling in this case is apparently rather than actually reduced since the expanding region does not exert much force against the surrounding medium. This reduces the ordinary thermal expansion generation of acoustic waves.